

Magneto-Optics of Anisotropic Exciton Polaritons in Two-Dimensional Perovskites

Jonas K. König,^{*} Jamie M. Fitzgerald, and Ermin Malic

Fachbereich Physik, Philipps-Universität, Marburg, 35032, Germany

E-mail: jonas.koenig@physik.uni-marburg.de

Abstract

Layered 2D organic–inorganic perovskite semiconductors support strongly confined excitons that offer significant potential for ultrathin polaritonic devices due to their tunability and huge oscillator strength. The application of a magnetic field has proven to be an invaluable tool for investigating the exciton fine structure observed in these materials. Yet, the combination of an in-plane magnetic field and the strong coupling regime has remained largely unexplored. In this work, we combine microscopic theory with a rigorous solution of Maxwell’s equations to model the magneto-optics of exciton polaritons in 2D perovskites. We predict that the brightened dark exciton state can enter the strong coupling regime. Furthermore, the magnetic-field-induced mixing of polarization selection rules and the breaking of in-plane symmetry lead to highly anisotropic polariton branches. This study contributes to a better understanding of the exciton fine structure in 2D perovskites and demonstrates the cavity control of highly anisotropic and polarization-sensitive exciton polaritons.

Keywords

exciton polaritons; dark excitons; anisotropic polaritons; magneto polaritons; 2D perovskites

Introduction

Layered 2D hybrid organic-inorganic metal halide perovskites have attracted a great deal of interest in recent years due to their improved environmental stability and superior tunability compared to their conventional 3D counterparts^{1,2}. They offer potential applications in ultrathin light emitters^{3,4}, photovoltaics^{5,6}, photodetectors⁷, and chiral optoelectronics⁸. Composed of an inorganic perovskite layer sandwiched between two layers of organic spacers acting as potential barriers, they form intrinsic 2D quantum well heterostructures⁹. These naturally stack on top of one another to form a single crystal slab, significantly enhancing the light-matter interaction through collective effects without modifying electronic properties¹⁰, in contrast to transition metal dichalcogenides¹¹. Their remarkable optical properties are governed by tightly bound excitons confined to the plane of the inorganic layer¹², and exhibit a rich exciton fine structure that comprises bright triplet and dark singlet states^{13,14}. Application of a twist angle¹⁵ and modification of the organic spacer¹⁶ have recently been shown to provide a tunable exciton oscillator strength and spacing, respectively. Emission studies of both nanocrystal and 2D lead-iodide perovskites have revealed deviations of the exciton distribution from Boltzmann statistics, resulting in surprisingly intense emission from higher-energy bright states even at cryogenic temperatures¹⁷⁻¹⁹. This is a direct consequence of an exciton relaxation bottleneck caused by a mismatch between the dark-bright exciton splitting and the energy of the involved optical phonons²⁰. There has been controversy in the literature regarding the energetic ordering of the dark and lowest bright states^{21,22}. The application of magneto-optical spectroscopy has played a key role in this debate, as it enables the direct observation of the dark state through the mixing of the singlet with a neighboring bright triplet state^{18-20,23,24}.

The large oscillator strength of their bright excitons, resulting from quantum and dielectric confinement, makes 2D metal-halide perovskites exceptional candidates for room-temperature exciton polaritonics²⁵. The strong coupling regime, with Rabi splittings in the range of hundreds of meV, has been achieved for perovskites integrated as active layers

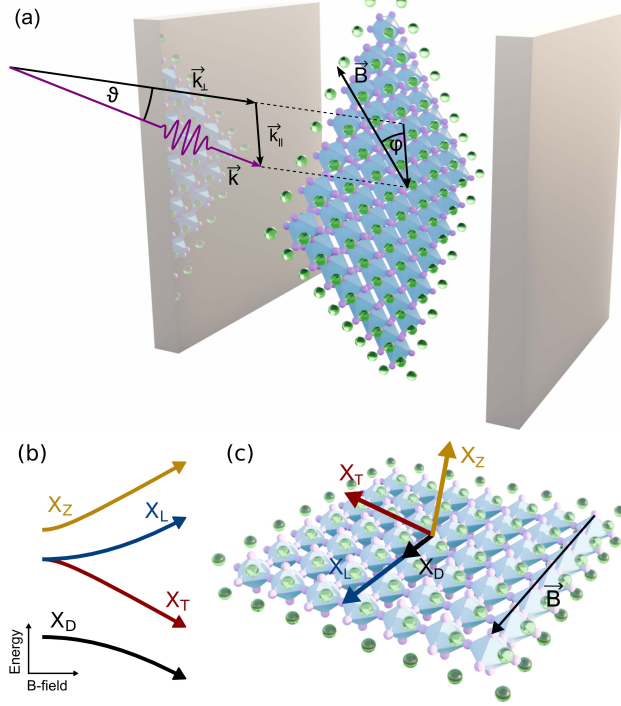


Figure 1: (a) Schematic figure of a 2D PEA_2PbI_4 perovskite slab integrated within a Fabry-Pérot cavity. The photon (purple arrow) is incident at an angle ϑ and momentum \mathbf{k} , where \mathbf{k}_\perp (\mathbf{k}_\parallel) denote the perpendicular (parallel) component with respect to the perovskite layer. There is an in-plane magnetic field \mathbf{B} with an azimuth angle φ relative to \mathbf{k}_\parallel . (b) Magnetic field dependence of the four exciton fine structure states: the dark (X_D), the two bright (X_T , X_L), and the gray exciton (X_Z). (c) Direction of the corresponding transition dipole moment for the four states in the presence of a magnetic field. While X_D and X_L are longitudinally polarized, X_T and X_Z are transversally polarized with respect to the magnetic field. The arrow length denotes the respective magnitude of the oscillator strength.

with planar microcavities^{26–29}, plasmonic structures^{30,31}, as well as cavity-free self-hybridized slabs^{28,32,33} and photonic crystals/metasurfaces^{34–36}. Interesting cavity physics has already been explored, including polariton bottlenecks²⁹, topological polaritons^{37,38}, the optical spin Hall effect³⁹, and polariton lasing³⁴ and condensation^{35,40}. In addition, combining polaritonics with the application of a magnetic field has been used to tune the Berry curvature of exciton polariton bands⁴¹, and, in general, provides interesting opportunities for anisotropic polaritonics⁴² via the breaking of in-plane symmetry. The brightening of the dark fine structure exciton¹⁹ makes it relevant for photonics, offering the potential for cavity control of spin⁴³, polarization^{24,44}, and directional transport^{36,45}: crucial ingredients for many quan-

tum optoelectronic applications²³. The photonic hybridization of different exciton states, both with and without an applied magnetic field, presents an exciting strategy to control, characterize, and visualize the still-debated exciton fine structure in 2D perovskites.

Based on a microscopic, material-specific, and predictive many-particle theory, we investigate the exciton fine structure of exemplary layered (PEA)₂PbI₄ perovskites⁴⁶, consisting of a *single* lead-iodide perovskite layer sandwiched between two layers of phenylethylammonium as organic spacers. We combine the Wannier equation, which provides microscopic access to exciton characteristics, with a full-wave solution of Maxwell's equations to describe exciton polaritons in 2D perovskites integrated within a Fabry-Pérot microcavity. Employing an in-plane magnetic field gives rise to rich optical selection rules, brightening the dark state¹⁹ and even potentially enabling it to enter the strong coupling regime. We study the effects of the magnetic field in terms of Rabi splitting and absorption of the polariton landscape. In particular, we observe interesting superimposed anisotropic polariton branches due to the magnetic field breaking the in-plane symmetry. Our work provides a first prediction of the magneto-absorption of exciton polaritons in 2D perovskites formed from the brightened dark state, highlighting their experimental signatures and tunability using the magnetic field strength and cavity length. This has relevance for potential ultrathin and tunable polarization-sensitive photonic devices, as well as for the characterization and visualization of the still-unresolved exciton fine structure in 2D perovskites.

Results and discussions

Theoretical Approach

To obtain the exciton energy landscape, we first solve the Wannier equation²⁰, which provides microscopic access to excitonic wavefunctions and binding energies. The short- and long-range exchange interaction between the electrons and holes is then converted to the exciton picture, and the resulting Hamiltonian is diagonalized (see SI for further details). This

results in an exciton fine structure energy landscape, including rich optical selection rules²⁰. With this approach, we are able to accurately describe previously observed features of the exciton fine structure of a 2D (PEA)₂PbI₄ perovskite layer^{19,24,47}. To model the optics of the perovskite layer, both in vacuum and within a Fabry-Pérot microcavity, we solve Maxwell's equations using the scattering matrix (S-matrix) method, which is suitable for layered media that are spatially homogeneous in the plane⁴⁸ (see SI). Excitons and their selection rules are included via a dispersive and anisotropic dielectric tensor

$$\varepsilon(\omega) = \begin{pmatrix} \varepsilon_B + \chi_x(\omega) & 0 & 0 \\ 0 & \varepsilon_B + \chi_y(\omega) & 0 \\ 0 & 0 & \varepsilon_B \end{pmatrix}, \quad (1)$$

with ε_B being the dielectric background of the perovskite, and $\chi_{x(y)}$ the frequency-dependent response function of the material in the in-plane $x(y)$ -direction. The latter is given by⁴⁹

$$\chi_{x(y)} \propto \sum_{\mu} \frac{\hbar\gamma_{\mu}^{x(y)}(\vartheta = 0^{\circ})}{(E_{\mu} - \hbar\omega) - i\hbar\Gamma_{\mu}}, \quad (2)$$

where E_{μ} is the energy of the μ th exciton and $\hbar\Gamma_{\mu}$ the corresponding exciton scattering rate. $\hbar\gamma_{\mu}^{x(y)}$ is the corresponding exciton radiative decay in the $x(y)$ -direction, which determines the oscillator strength (Fig. S1 in the SI). Changing the momentum components of the incoming photon allows us to vary both the angle of incidence, ϑ , and the azimuth angle, φ , with respect to the magnetic field, as shown in Fig. 1(a). For simplicity, we focus only on TE-polarized light, i.e., where the polarization of the light is purely in the xy -plane, and the excitonic contribution from the out-of-plane z -component can be ignored.

We consider a microcavity consisting of a pair of Bragg mirrors, with a single perovskite quantum well in the center (Fig.1). Using the S-matrix method, with microscopic input from the Wannier equation, we calculate the linear optical spectra of the combined system. While this provides exact solutions to Maxwell's equations, it does not give access to the Hopfield

coefficients, which are necessary for a detailed understanding of the constituent nature and decay channels of each polariton^{50,51}. We therefore extract the exciton polariton energies from the calculated reflection, and the resulting dispersion manifolds are then fitted to a two-exciton-one-photon Hopfield model^{50,52}. This provides microscopic access to the cavity photon-exciton coupling strength, g_μ , and the Hopfield coefficients, U_μ^n . The Hopfield matrix is given by

$$H = \begin{pmatrix} E^{(C)} & g_1 & g_2 \\ g_1 & E_1^{(X)} & 0 \\ g_2 & 0 & E_2^{(X)} \end{pmatrix}, \quad (3)$$

where $E_\mu^{(X)}$ is the energy of the μ th exciton and $E^{(C)}$ denotes the energy of the bare cavity photon, which is extracted from an S-matrix simulation ignoring excitonic effects.

To further analyze the results, we use coupled mode theory, which is appropriate for describing the coupling of low-loss material resonances and high-Q photonic modes to each other and to external ports⁵³ (see the SI). The absorption of a single resonator (valid for excitons or polaritons) is given by the Elliott formula^{49,50}

$$A(\omega) = \frac{2\hbar\Gamma\hbar\gamma}{(\hbar\omega_R - \hbar\omega)^2 + (\hbar\Gamma + \hbar\gamma)^2}, \quad (4)$$

with ω_R being the frequency of the respective resonator, while $\hbar\gamma$ and $\hbar\Gamma$ are the photonic and material-based decay channels, respectively. For a symmetric system excited from one port, the absorption has an upper bound⁵⁴ of 0.5, which is reached at the critical coupling condition^{51,55} of $\gamma = \Gamma$, as can be seen from Eq. (4).

Exciton fine structure and magneto-absorption

We use the approach presented above to investigate the exciton fine structure and absorption in 2D perovskites under an applied in-plane magnetic field, both with and without

integration into a Fabry-Pérot cavity. Solving the Wannier equation, we obtain a binding energy of approximately 220 meV for the four-fold degenerate exciton, originating from the possible spin configurations of electrons and holes¹⁴: in excellent agreement with prior theoretical^{20,56} and experimental^{46,57} studies. Including the exchange interaction, we find that the four degenerate spin states split in energy. The energetically lowest singlet state is optically dark^{18,19} and is therefore labeled the dark state, X_D . Furthermore, there are two degenerate circularly polarized bright states, $X_{T/L}$, and an out-of-plane polarized gray state, X_Z ^{10,47}. If an in-plane magnetic field is applied (Voigt configuration), these states further mix, modifying their energy and optical selection rules¹⁹. Their energy shift as a function of the magnetic field strength is sketched in Fig. 1(b). Level repulsion causes the dark state to shift down in energy, the gray exciton to shift up, and the two degenerate bright states to split apart. The previously circularly polarized states become linearly polarized²⁴, where X_T is orthogonal (transversal) to the magnetic field but no longer fully in-plane, while X_L is parallel (longitudinal). Furthermore, the dark state brightens and becomes polarized along the magnetic field direction due to field-induced mixing with the X_L state as a consequence of the spin selection rules⁵⁸. Lastly, the gray state is also transversally polarized, but it is no longer strictly orientated out-of-plane due to mixing with the X_T state. The orientation of the transition dipole moments with respect to the B -field is illustrated in Fig. 1(c).

According to these selection rules, when the bare perovskite slab is excited with TE-polarized light in the absence of a magnetic field, the response is independent of the azimuth angle φ and only a single absorption peak at the energy of the degenerate bright states is observed. In contrast, in the presence of a high magnetic field, the optical response depends crucially on φ . For $\varphi = 0^\circ$ (i.e., when the electric field of the light is fully in-plane and orthogonal to the applied magnetic field), only the transversal states, X_T and X_Z , can couple to the light via their in-plane component¹⁹. Considering a magnetic field strength of 50 T, this leads to two absorption peaks at low angles of incidence, as illustrated in Fig. 2(a). For higher angles of ϑ , the two peaks merge and there is a strong absorption approximately

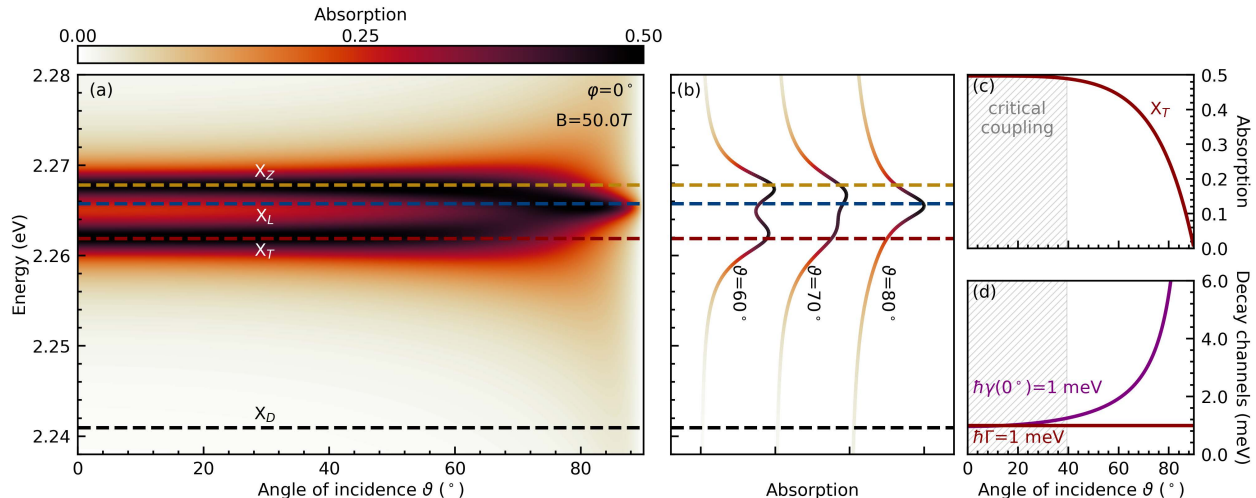


Figure 2: (a) Absorption of a 2D PEA_2PbI_4 perovskite layer as a function of photon energy and angle of incidence for $B = 50$ T and $\varphi = 0^\circ$. The horizontal dashed lines indicate the energies of the four exciton fine structure states. As we consider TE-polarized light, i.e., a polarization perpendicular to the magnetic field at $\varphi = 0^\circ$, only X_T and X_Z excitons can couple to light at this orientation, as shown in Fig. 1(c). (b) Line cuts of the absorption spectrum at specific higher angles of incidence. (c) Absorption along the energy of X_T . (d) Radiative ($\hbar\gamma$) and material-based ($\hbar\Gamma$) decay channels for X_T . The shaded area indicates where the two decay channels have a relative difference of less than 5%, marking the critical coupling region with maximal absorption.

at the X_L energy. A closer analysis of the two peaks reveals that they broaden and overlap, creating the impression of a single peak between them that coincides with X_L , as illustrated in Fig. 2(b). For TE-polarized light, the radiative decay $\hbar\gamma_\mu$ of a given exciton state μ can be shown to scale with⁵⁹ $1/\cos(\vartheta)$ and thus diverges as ϑ limits towards 90° ⁶⁰. Consequently, the full width at half maximum of the peak, given by $2(\hbar\Gamma_\mu + \hbar\gamma_\mu)$, also increases rapidly as ϑ approaches grazing angles. Surprisingly, as the radiative decay of the exciton diverges, the absorption decreases to zero, as shown in Fig. 2(c). This occurs because the difference between radiative and material-based decay rates increases with ϑ (Fig. 2(d)), moving the system away from the critical coupling regime and therefore decreasing the absorption.

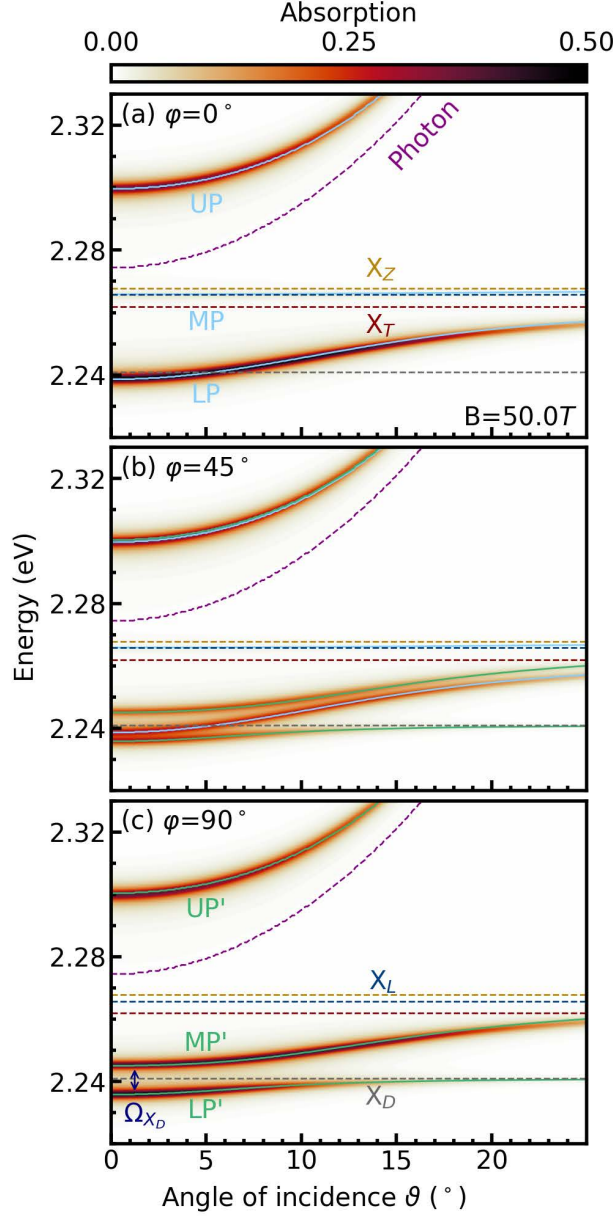


Figure 3: (a)-(c) Absorption of a 2D $(\text{PEA})_2\text{PbI}_4$ perovskite layer integrated within a Fabry-Pérot microcavity as a function of the photon energy and angle of incidence for $B = 50 \text{ T}$ and different azimuth angles φ . The horizontal dashed lines indicate the exciton energies. Depending on φ , different polariton branches (denoted by LP, MP, and UP for $\varphi = 0^\circ$ and LP', MP', and UP' for $\varphi = 90^\circ$) appear as a result of the selection rules of the respective excitonic states. The small vertical arrow in part (c) denotes the Rabi splitting of the dark state, Ω_{X_D} , which brightens in the presence of a magnetic field.

Polariton magneto-absorption in an optical cavity

The integration of a perovskite slab into a microcavity, combined with the brightening of the dark state in the presence of an in-plane magnetic field, presents a potential strategy to

investigate the still-debated energetic ordering of the exciton fine structure states in these materials. Furthermore, the anisotropy induced by the magnetic field is expected to have a dramatic impact on polariton optics. In particular, by varying the azimuth angle φ , the projection of the electric field onto the transition dipole moment of the various fine structure states can be altered relative to the applied in-plane magnetic field orientation, leading to a rich anisotropic polariton dispersion that can be selectively probed with the incident beam angle. The polariton landscape in the absence of the magnetic field is discussed in the SI. Here, we focus on the case of magneto-optics. Starting with $\varphi = 0^\circ$, where the electric field is orientated perpendicular to the applied magnetic field, only the two excitons, X_T and X_Z , can couple to the incident laser, similar to the bare perovskite case. This results in three polariton branches, a lower (LP), middle (MP) and upper polariton branch (UP), cf. Fig.3(a). As the middle branch is sandwiched between the almost energetically degenerate states X_T and X_Z , it is nearly flat and therefore barely visible in absorption⁵⁰. As a result, only one large apparent Rabi splitting is observed, instead of the two splittings typically observed for a two-exciton, one-photon system. However, the absorption of the middle branch increases with stronger magnetic fields as the separation between X_T and X_Z grows.

For $\varphi = 90^\circ$, where the electric field is orientated parallel to the applied magnetic field, only X_L and X_D can couple to the light. This leads again to three polariton branches (LP', MP', UP'), cf. Fig. 3(c). As X_L and X_D are well separated in energy, the middle polariton is no longer flat, and we observe two Rabi splittings: one around X_L and a smaller splitting around X_D . The latter is labeled as Ω_{X_D} and defined as the difference between LP' and MP' at $\vartheta = 0^\circ$. The upper polariton branch (UP) is approximately independent of φ and hence very similar for the 0° and 90° cases. This is because the combined oscillator strength of X_Z and X_T is approximately equal to that of X_L , due to the conservation of oscillator strength in the presence of Zeeman splitting²⁰.

Applying a fit using the Hopfield model (Eq. (3)) gives a Rabi splitting of $\Omega_{X_D} = 9 \text{ meV}$ for the dark state at $B = 50 \text{ T}$, while for X_L the splitting is 54 meV . In comparison, the

Rabi splitting of the X_T and X_Z states in the $\varphi = 0^\circ$ case is 60 meV. The detuning was chosen such that the LP in Fig. 3(a) coincides approximately with the dark state, leading to a Rabi splitting around the dark state, Ω_{X_D} , to be at $\vartheta = 0^\circ$, as indicated by the small vertical arrow in Fig. 3(c). Smaller cavity lengths would increase the energy of the cavity photon mode, thereby detuning the cavity from the X_D energy and leading to a smaller Rabi splitting. In contrast, a longer cavity length would decrease the cavity photon energy, shifting the Rabi splitting to larger angles of incidence. These results constitute a first prediction that, at certain incident laser orientations, the brightened low-energy dark state can enter the strong coupling regime and be observed by magneto-optical measurements. This paves the way towards cavity control of the exciton fine structure in 2D perovskites.

Interestingly, at an intermediate angle of $\varphi = 45^\circ$, we do not observe a smaller Rabi splitting around the brightened dark state (Fig. 3(b)), as might be naively expected from considering only the projection of the oscillator strength. Instead, we observe a superposition of the two previously discussed limiting cases of $\varphi = 0^\circ$ and $\varphi = 90^\circ$, with unchanged Rabi splittings but altered absorption. The upper branch still has the same absorption due to the near-degeneracy of UP and UP', while the other branches have their absorption approximately halved. This behavior of superimposed Rabi splittings is related to a magnetic-field-induced anisotropy of the dielectric tensor, which arises from the two inequivalent dipoles pointing in different directions. Similar results have previously been observed in orientated molecular aggregates⁶¹ and 2D naturally anisotropic TMD (ReS₂) layers⁶². In the Hopfield model, this means that there are two degenerate cavity modes polarized orthogonal to each other, which oscillate perpendicular (parallel) to the magnetic field and couple only to X_T and X_Z (only to X_D and X_L). Therefore, this six-branch system decouples into two three-branch subsystems, orientated perpendicular and parallel to the magnetic field, respectively, and exhibiting the same cavity-exciton couplings as before. The observed magnetic field and cavity control of the polariton landscape, particularly the modification of the Rabi splitting relative to typical phonon energies, presents opportunities to manipulate optics^{56,63} and relaxation

in these materials^{20,64}, with relevance, e.g., to polariton lasing⁶⁵. The anisotropic polariton bands will lead to a direction-dependent relaxation, with the middle polariton branch anticipated to play an important role in dictating relaxation from higher-energy states to the lower polariton branch⁶⁶.

Tunability of Rabi splitting and absorption intensity

Now, we explore the tunability of the system with respect to the applied in-plane magnetic field. With increasing field strength, oscillator strength is transferred from X_L to X_D (see SI). Therefore, the Rabi splitting Ω_{X_D} around the dark state is also expected to grow. We find that Ω_{X_D} scales linearly with the magnetic field, cf. Fig. 4(a). The oscillator strength of the dark state scales quadratically with the magnetic field, provided that the Zeeman splitting $\mu_B B$ is small compared to the energy difference between the X_L and X_D states⁵⁸. Furthermore, the coupling between exciton and cavity photon modes is proportional to the square root of the oscillator strength⁵⁰, explaining the observed linear behavior. The absorption as a function of the magnetic field strength is provided in the SI.

Another way to tune the system is to change the exciton linewidth $\hbar\Gamma$ via, e.g., varying the temperature⁵⁶. The material-based loss of a polariton branch n is given by the sum of the linewidths of all its excitonic components, weighted by the respective excitonic Hopfield coefficients $\hbar\Gamma_n^{(P)} = \sum_\mu \hbar\Gamma (U_\mu^n)^2$ ^{50,51}. Similarly, the radiative decay is given by the cavity mode linewidth, $\hbar\kappa$, scaled by the photonic Hopfield coefficient $\hbar\gamma_n^{(P)} = \hbar\kappa (U_0^n)^2$. The different branches in Fig. 3(a) reach a large absorption at $\vartheta = 0^\circ$ for different $\hbar\Gamma$, as illustrated in Fig. 4(b). For a particular polariton branch, we find that high absorption coincides with regions where the respective excitonic and photonic loss rates are similar (Figs. 4(c)-(d)), i.e., fulfilling the critical coupling condition that is contained in Eq. (4)^{50,51}. For the $\varphi = 90^\circ$ case, we find qualitatively the same results (Figs. 4(e)-(g)), with the main distinction from the 0° case being the different Hopfield coefficients, i.e., different light-matter compositions of the polariton branches. A plot of the Hopfield coefficients as a function of the angle of

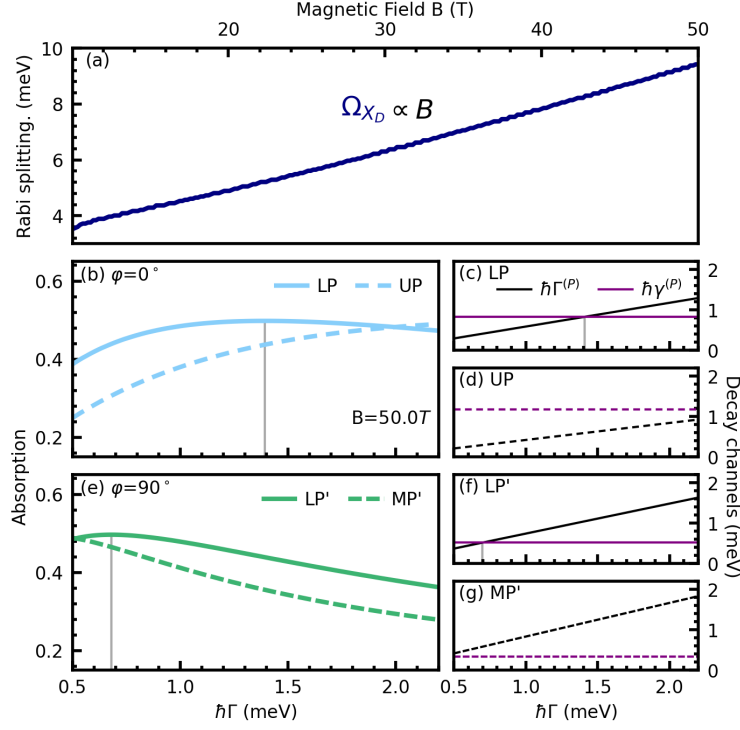


Figure 4: (a) Rabi splitting, Ω_{X_D} , stemming from the avoided crossing between the dark state and the photon energy, as a function of the magnetic field strength B (see the arrow in Fig. 3(c)). (b) Resonant absorption of the lower (LP) and upper (UP) polariton branches from 3(a) ($\varphi = 0^\circ$) at $\vartheta = 0^\circ$ as a function of the excitonic linewidth $\hbar\Gamma$. The vertical gray line indicates the point where the absorption reaches a peak value of 0.5. (c)-(d) Photonic, $\hbar\gamma^{(P)}$, and excitonic, $\hbar\Gamma^{(P)}$, decay channels of the polariton branches LP and UP, respectively. The vertical gray line shows where the two are equal, i.e., the critical coupling condition is met. It coincides exactly with the vertical gray line in (b). (e) The same plot as in (b), but for $\varphi = 90^\circ$, illustrating the lower (LP') and the middle (MP') polariton branches from Fig. 3(c). (f)-(g) Photonic and excitonic decay channels of the corresponding polariton branches LP' and MP', respectively.

incidence can be found in the SI. These results reveal how a combination of magneto-optical measurements and modeling using the Hopfield method and Elliott formula can unravel the interplay of optical selection rules and the balance of decay channels that determine the optical response of exciton polaritons in 2D perovskites.

Conclusions

We have revealed the rich magneto-optical response of dark and bright exciton states in 2D perovskites, both in vacuum and when integrated within a Fabry-Pérot microcavity. In particular, we show that the dark state can enter the strong coupling regime under an applied in-plane magnetic field. Furthermore, we predict anisotropic polariton manifolds in 2D perovskites arising from a magnetic field-induced anisotropy. We also demonstrate that the dispersion and the absorption of different polariton branches can be tuned by adjusting the azimuth angle of the light beam relative to the magnetic field. These gained insights contribute to a deeper microscopic understanding of exciton polaritons in 2D perovskites and could also be important for technologically relevant directional tuning and polarization control of both polariton transport and emission.

Supporting Information Available

Details on the derivation of the main equations and additional discussion of the magnetic-field-dependent polariton landscape (PDF)

Acknowledgement

We acknowledge funding from the DFG via SFB 1083 and the regular project 524612380. We also want to thank Joshua Thompson (University of Cambridge) and Ellie Kraus (Phillips-Universität Marburg) for their valuable discussion as well as Giuseppe Meneghini (Phillips-Universität Marburg) for his help with Figure 1(a).

References

- (1) Pedesseau, L.; Saponi, D.; Traore, B.; Robles, R.; Fang, H.-H.; Loi, M. A.; Tsai, H.; Nie, W.; Blancon, J.-C.; Neukirch, A.; others Advances and promises of layered halide hybrid perovskite semiconductors. *ACS nano* **2016**, *10*, 9776–9786.
- (2) Chen, Y.; Sun, Y.; Peng, J.; Tang, J.; Zheng, K.; Liang, Z. 2D Ruddlesden–Popper perovskites for optoelectronics. *Advanced Materials* **2018**, *30*, 1703487.
- (3) Dou, L.; Wong, A. B.; Yu, Y.; Lai, M.; Kornienko, N.; Eaton, S. W.; Fu, A.; Bischak, C. G.; Ma, J.; Ding, T.; others Atomically thin two-dimensional organic-inorganic hybrid perovskites. *Science* **2015**, *349*, 1518–1521.
- (4) Hu, H.; Salim, T.; Chen, B.; Lam, Y. M. Molecularly engineered organic-inorganic hybrid perovskite with multiple quantum well structure for multicolored light-emitting diodes. *Scientific reports* **2016**, *6*, 33546.
- (5) Tsai, H.; Nie, W.; Blancon, J.-C.; Stoumpos, C. C.; Asadpour, R.; Harutyunyan, B.; Neukirch, A. J.; Verduzco, R.; Crochet, J. J.; Tretiak, S.; others High-efficiency two-dimensional Ruddlesden–Popper perovskite solar cells. *Nature* **2016**, *536*, 312–316.
- (6) Chen, Y.; Sun, Y.; Peng, J.; Zhang, W.; Su, X.; Zheng, K.; Pullerits, T.; Liang, Z. Tailoring organic cation of 2D air-stable organometal halide perovskites for highly efficient planar solar cells. *Advanced Energy Materials* **2017**, *7*, 1700162.
- (7) Zhou, J.; Chu, Y.; Huang, J. Photodetectors based on two-dimensional layer-structured hybrid lead iodide perovskite semiconductors. *ACS applied materials & interfaces* **2016**, *8*, 25660–25666.
- (8) Liu, S.; Kepenekian, M.; Bodnar, S.; Feldmann, S.; Heindl, M. W.; Fehn, N.; Zerhoch, J.; Shcherbakov, A.; Pöthig, A.; Li, Y.; others Bright circularly polarized photo-

- luminescence in chiral layered hybrid lead-halide perovskites. *Science Advances* **2023**, *9*, eadh5083.
- (9) Stoumpos, C. C.; Cao, D. H.; Clark, D. J.; Young, J.; Rondinelli, J. M.; Jang, J. I.; Hupp, J. T.; Kanatzidis, M. G. Ruddlesden–Popper hybrid lead iodide perovskite 2D homologous semiconductors. *Chemistry of Materials* **2016**, *28*, 2852–2867.
- (10) Fieramosca, A.; De Marco, L.; Passoni, M.; Polimeno, L.; Rizzo, A.; Rosa, B. L.; Cruciani, G.; Dominici, L.; De Giorgi, M.; Gigli, G.; others Tunable out-of-plane excitons in 2D single-crystal perovskites. *Acs Photonics* **2018**, *5*, 4179–4185.
- (11) Liu, X.; Galfsky, T.; Sun, Z.; Xia, F.; Lin, E.-c.; Lee, Y.-H.; Kéna-Cohen, S.; Menon, V. M. Strong light–matter coupling in two-dimensional atomic crystals. *Nature Photonics* **2015**, *9*, 30–34.
- (12) Blancon, J.-C.; Stier, A. V.; Tsai, H.; Nie, W.; Stoumpos, C. C.; Traore, B.; Pedesseau, L.; Kepenekian, M.; Katsutani, F.; Noe, G.; others Scaling law for excitons in 2D perovskite quantum wells. *Nature communications* **2018**, *9*, 2254.
- (13) Tanaka, K.; Takahashi, T.; Kondo, T.; Umeda, K.; Ema, K.; Umebayashi, T.; Asai, K.; Uchida, K.; Miura, N. Electronic and excitonic structures of inorganic–organic perovskite-type quantum-well crystal (C₄H₉NH₃)₂PbBr₄. *Japanese journal of applied physics* **2005**, *44*, 5923.
- (14) Baranowski, M.; Plochocka, P. Excitons in metal-halide perovskites. *Advanced Energy Materials* **2020**, *10*, 1903659.
- (15) Zhang, S.; Jin, L.; Lu, Y.; Zhang, L.; Yang, J.; Zhao, Q.; Sun, D.; Thompson, J. J.; Yuan, B.; Ma, K.; others Moiré superlattices in twisted two-dimensional halide perovskites. *Nature Materials* **2024**, 1–8.

- (16) Dyksik, M.; Baranowski, M.; Thompson, J. J.; Yang, Z.; Medina, M. R.; Loi, M. A.; Malic, E.; Plochocka, P. Steric Engineering of Exciton Fine Structure in 2D Perovskites. *Advanced Energy Materials* **2024**, 2404769.
- (17) Xu, K.; Vliem, J. F.; Meijerink, A. Long-lived dark exciton emission in Mn-doped CsPbCl₃ perovskite nanocrystals. *The Journal of Physical Chemistry C* **2018**, *123*, 979–984.
- (18) Tamarat, P.; Bodnarchuk, M. I.; Trebbia, J.-B.; Erni, R.; Kovalenko, M. V.; Even, J.; Lounis, B. The ground exciton state of formamidinium lead bromide perovskite nanocrystals is a singlet dark state. *Nature materials* **2019**, *18*, 717–724.
- (19) Dyksik, M.; Duim, H.; Maude, D. K.; Baranowski, M.; Loi, M. A.; Plochocka, P. Brightening of dark excitons in 2D perovskites. *Science advances* **2021**, *7*, eabk0904.
- (20) Thompson, J. J.; Dyksik, M.; Peksa, P.; Posmyk, K.; Joki, A.; Perea-Causin, R.; Erhart, P.; Baranowski, M.; Loi, M. A.; Plochocka, P.; others Phonon-Bottleneck Enhanced Exciton Emission in 2D Perovskites. *Advanced Energy Materials* **2024**, *14*, 2304343.
- (21) Becker, M. A.; Vaxenburg, R.; Nedelcu, G.; Sercel, P. C.; Shabaev, A.; Mehl, M. J.; Michopoulos, J. G.; Lambrakos, S. G.; Bernstein, N.; Lyons, J. L.; others Bright triplet excitons in caesium lead halide perovskites. *Nature* **2018**, *553*, 189–193.
- (22) Lou, X.; Li, Y.; Lei, H.; Zhang, Y.; Zhou, H.; Shi, E.; Zhu, H. Robust and Efficient Out-of-Plane Exciton Transport in Two-Dimensional Perovskites via Ultrafast Förster Energy Transfer. *ACS nano* **2024**, *18*, 20659–20666.
- (23) Tamarat, P.; Hou, L.; Trebbia, J.-B.; Swarnkar, A.; Biadala, L.; Louyer, Y.; Bodnarchuk, M. I.; Kovalenko, M. V.; Even, J.; Lounis, B. The dark exciton ground state promotes photon-pair emission in individual perovskite nanocrystals. *Nature communications* **2020**, *11*, 6001.

- (24) Posmyk, K.; Zawadzka, N.; Dyksik, M.; Surrente, A.; Maude, D. K.; Kazimierczuk, T.; Babiński, A.; Molas, M. R.; Paritmongkol, W.; Mączka, M.; others Quantification of exciton fine structure splitting in a two-dimensional perovskite compound. *The Journal of Physical Chemistry Letters* **2022**, *13*, 4463–4469.
- (25) Su, R.; Fieramosca, A.; Zhang, Q.; Nguyen, H. S.; Deleporte, E.; Chen, Z.; Sanvitto, D.; Liew, T. C.; Xiong, Q. Perovskite semiconductors for room-temperature exciton-polaritonics. *Nature Materials* **2021**, *20*, 1315–1324.
- (26) Lanty, G.; Brehier, A.; Parashkov, R.; Lauret, J.-S.; Deleporte, E. Strong exciton–photon coupling at room temperature in microcavities containing two-dimensional layered perovskite compounds. *New Journal of Physics* **2008**, *10*, 065007.
- (27) Wang, J.; Su, R.; Xing, J.; Bao, D.; Diederichs, C.; Liu, S.; Liew, T. C.; Chen, Z.; Xiong, Q. Room temperature coherently coupled exciton–polaritons in two-dimensional organic–inorganic perovskite. *ACS nano* **2018**, *12*, 8382–8389.
- (28) Fieramosca, A.; Polimeno, L.; Ardizzone, V.; De Marco, L.; Pugliese, M.; Maiorano, V.; De Giorgi, M.; Dominici, L.; Gigli, G.; Gerace, D.; others Two-dimensional hybrid perovskites sustaining strong polariton interactions at room temperature. *Science advances* **2019**, *5*, eaav9967.
- (29) Laitz, M.; Kaplan, A. E.; Deschamps, J.; Barotov, U.; Proppe, A. H.; García-Benito, I.; Osherov, A.; Grancini, G.; deQuilettes, D. W.; Nelson, K. A.; others Uncovering temperature-dependent exciton-polariton relaxation mechanisms in hybrid organic-inorganic perovskites. *Nature Communications* **2023**, *14*, 2426.
- (30) Symonds, C.; Bellessa, J.; Plenet, J.; Bréhier, A.; Parashkov, R.; Lauret, J.; Deleporte, E. Emission of hybrid organic-inorganic exciton/plasmon mixed states. *Applied Physics Letters* **2007**, *90*.

- (31) Niu, W.; Ibbotson, L. A.; Leipold, D.; Runge, E.; Prakash, G. V.; Baumberg, J. J. Image excitons and plasmon-exciton strong coupling in two-dimensional perovskite semiconductors. *Physical Review B* **2015**, *91*, 161303.
- (32) Anantharaman, S. B.; Stevens, C. E.; Lynch, J.; Song, B.; Hou, J.; Zhang, H.; Jo, K.; Kumar, P.; Blancon, J.-C.; Mohite, A. D.; others Self-hybridized polaritonic emission from layered perovskites. *Nano Letters* **2021**, *21*, 6245–6252.
- (33) Anantharaman, S. B.; Lynch, J.; Stevens, C. E.; Munley, C.; Li, C.; Hou, J.; Zhang, H.; Torma, A.; Darlington, T.; Coen, F.; others Dynamics of self-hybridized exciton–polaritons in 2D halide perovskites. *Light: Science & Applications* **2024**, *13*, 1.
- (34) Masharin, M. A.; Samusev, A.; Bogdanov, A.; Iorsh, I.; Demir, H. V.; Makarov, S. Room-Temperature Exceptional-Point-Driven Polariton Lasing from Perovskite Metasurface. *Advanced Functional Materials* **2023**, *33*, 2215007.
- (35) Wu, X.; Zhang, S.; Song, J.; Deng, X.; Du, W.; Zeng, X.; Zhang, Y.; Zhang, Z.; Chen, Y.; Wang, Y.; others Exciton polariton condensation from bound states in the continuum at room temperature. *Nature Communications* **2024**, *15*, 3345.
- (36) Dang, N. H. M.; Zanotti, S.; Drouard, E.; Chevalier, C.; Trippé-Allard, G.; Deleporte, E.; Seassal, C.; Gerace, D.; Nguyen, H. S. Long-Range Ballistic Propagation of 80% Excitonic Fraction Polaritons in a Perovskite Metasurface at Room Temperature. *Nano Letters* **2024**, *24*, 11839–11846.
- (37) Su, R.; Ghosh, S.; Liew, T. C.; Xiong, Q. Optical switching of topological phase in a perovskite polariton lattice. *Science Advances* **2021**, *7*, eabf8049.
- (38) Jin, F.; Mandal, S.; Wu, J.; Zhang, Z.; Wen, W.; Ren, J.; Zhang, B.; Liew, T. C.; Xiong, Q.; Su, R. Observation of perovskite topological valley exciton-polaritons at room temperature. *Nature Communications* **2024**, *15*, 1–8.

- (39) Shi, Y.; Gan, Y.; Chen, Y.; Wang, Y.; Ghosh, S.; Kavokin, A.; Xiong, Q. Coherent optical spin Hall transport for polaritonics at room temperature. *Nature Materials* **2024**, 1–7.
- (40) Su, R.; Ghosh, S.; Wang, J.; Liu, S.; Diederichs, C.; Liew, T. C.; Xiong, Q. Observation of exciton polariton condensation in a perovskite lattice at room temperature. *Nature Physics* **2020**, *16*, 301–306.
- (41) Polimeno, L.; Lerario, G.; De Giorgi, M.; De Marco, L.; Dominici, L.; Todisco, F.; Coriolano, A.; Ardizzone, V.; Pugliese, M.; Prontera, C. T.; others Tuning of the Berry curvature in 2D perovskite polaritons. *Nature nanotechnology* **2021**, *16*, 1349–1354.
- (42) Wang, H.; Kumar, A.; Dai, S.; Lin, X.; Jacob, Z.; Oh, S.-H.; Menon, V.; Narimanov, E.; Kim, Y. D.; Wang, J.-P.; others Planar hyperbolic polaritons in 2D van der Waals materials. *Nature communications* **2024**, *15*, 69.
- (43) Lu, H.; Xiao, C.; Song, R.; Li, T.; Maughan, A. E.; Levin, A.; Brunecky, R.; Berry, J. J.; Mitzi, D. B.; Blum, V.; others Highly distorted chiral two-dimensional tin iodide perovskites for spin polarized charge transport. *Journal of the American Chemical Society* **2020**, *142*, 13030–13040.
- (44) Wang, T.; Zang, Z.; Gao, Y.; Lyu, C.; Gu, P.; Yao, Y.; Peng, K.; Watanabe, K.; Taniguchi, T.; Liu, X.; others Electrically pumped polarized exciton-polaritons in a halide perovskite microcavity. *Nano Letters* **2022**, *22*, 5175–5181.
- (45) Voronin, K. V.; Álvarez-Pérez, G.; Lanza, C.; Alonso-González, P.; Nikitin, A. Y. Fundamentals of polaritons in strongly anisotropic thin crystal layers. *ACS Photonics* **2024**, *11*, 550–560.
- (46) Hong, X.; Ishihara, T.; Nurmikko, A. Dielectric confinement effect on excitons in PbI₄-based layered semiconductors. *Physical Review B* **1992**, *45*, 6961.

- (47) Posmyk, K.; Dyksik, M.; Surrente, A.; Maude, D. K.; Zawadzka, N.; Babiński, A.; Molas, M. R.; Paritmongkol, W.; Mączka, M.; Tisdale, W. A.; others Exciton Fine Structure in 2D Perovskites: The Out-of-Plane Excitonic State. *Advanced Optical Materials* **2024**, *12*, 2300877.
- (48) Rumpf, R. C. Improved formulation of scattering matrices for semi-analytical methods that is consistent with convention. *Progress In Electromagnetics Research B* **2011**, *35*, 241–261.
- (49) Kira, M.; Koch, S. W. Many-body correlations and excitonic effects in semiconductor spectroscopy. *Progress in quantum electronics* **2006**, *30*, 155–296.
- (50) Fitzgerald, J. M.; Thompson, J. J.; Malic, E. Twist angle tuning of moiré exciton polaritons in van der Waals heterostructures. *Nano Letters* **2022**, *22*, 4468–4474.
- (51) Ferreira, B.; Rosati, R.; Fitzgerald, J. M.; Malic, E. Signatures of dark excitons in exciton–polariton optics of transition metal dichalcogenides. *2D Materials* **2022**, *10*, 015012.
- (52) Hopfield, J. Theory of the contribution of excitons to the complex dielectric constant of crystals. *Physical Review* **1958**, *112*, 1555.
- (53) Fan, S.; Suh, W.; Joannopoulos, J. D. Temporal coupled-mode theory for the Fano resonance in optical resonators. *JOSA A* **2003**, *20*, 569–572.
- (54) Piper, J. R.; Liu, V.; Fan, S. Total absorption by degenerate critical coupling. *Applied Physics Letters* **2014**, *104*.
- (55) König, J. K.; Fitzgerald, J. M.; Hagel, J.; Erckensten, D.; Malic, E. Interlayer exciton polaritons in homobilayers of transition metal dichalcogenides. *2D Materials* **2023**, *10*, 025019.

- (56) Feldstein, D.; Perea-Causin, R.; Wang, S.; Dyksik, M.; Watanabe, K.; Taniguchi, T.; Plochocka, P.; Malic, E. Microscopic picture of electron–phonon interaction in two-dimensional halide perovskites. *The Journal of Physical Chemistry Letters* **2020**, *11*, 9975–9982.
- (57) Urban, J. M.; Chehade, G.; Dyksik, M.; Menahem, M.; Surrente, A.; Trippé-Allard, G.; Maude, D. K.; Garrot, D.; Yaffe, O.; Deleporte, E.; others Revealing excitonic phonon coupling in (PEA)₂(MA)_n-1Pb_nI_{3n+1} 2D layered perovskites. *The journal of physical chemistry letters* **2020**, *11*, 5830–5835.
- (58) Feierabend, M.; Brem, S.; Ekman, A.; Malic, E. Brightening of spin-and momentum-dark excitons in transition metal dichalcogenides. *2D Materials* **2020**, *8*, 015013.
- (59) Kavokin, A.; Kaliteevski, M. Excitonic light reflection and absorption in semiconductor microcavities at oblique incidence. *Solid state communications* **1995**, *95*, 859–862.
- (60) Creatore, C.; Ivanov, A. L. Strong and weak coupling limits in optics of quantum well excitons. *Physical Review B—Condensed Matter and Materials Physics* **2008**, *77*, 075324.
- (61) Balagurov, D.; La Rocca, G. Organic microcavities with anisotropic optically active materials. *physica status solidi (c)* **2004**, *1*, 518–521.
- (62) Chakrabarty, D.; Dhara, A.; Ghosh, K.; Pattanayak, A. K.; Mukherjee, S.; Chaudhuri, A. R.; Dhara, S. Interfacial anisotropic exciton-polariton manifolds in ReS₂. *Optica* **2021**, *8*, 1488–1494.
- (63) Ferreira, B.; Shan, H.; Rosati, R.; Fitzgerald, J. M.; Lackner, L.; Han, B.; Esmann, M.; Hays, P.; Leibelng, G.; Watanabe, K.; Taniguchi, T.; Eilenberger, F.; Tongay, S.; Schneider, C.; Malic, E. Revealing Dark Exciton Signatures in Polariton Spectra of 2D Materials. *ACS Photonics* **2024**, *11*, 2215–2220.

- (64) Fitzgerald, J. M.; Rosati, R.; Ferreira, B.; Shan, H.; Schneider, C.; Malic, E. Circumventing the polariton bottleneck via dark excitons in 2D semiconductors. *Optica* **2024**, *11*, 1346–1351.
- (65) Butté, R.; Delalleau, G.; Tartakovskii, A.; Skolnick, M.; Astratov, V.; Baumberg, J.; Malpuech, G.; Di Carlo, A.; Kavokin, A.; Roberts, J. Transition from strong to weak coupling and the onset of lasing in semiconductor microcavities. *Physical Review B* **2002**, *65*, 205310.
- (66) Hu, Z.; Krisnanda, T.; Fieramosca, A.; Zhao, J.; Sun, Q.; Chen, Y.; Liu, H.; Luo, Y.; Su, R.; Wang, J.; others Energy transfer driven brightening of MoS₂ by ultrafast polariton relaxation in microcavity MoS₂/hBN/WS₂ heterostructures. *Nature Communications* **2024**, *15*, 1747.

Supplementary Information

Magneto-Optics of Anisotropic Exciton Polaritons in Two-Dimensional Perovskites

Jonas K. König,^{*} Jamie M. Fitzgerald, and Ermin Malic

Fachbereich Physik, Philipps-Universität, Marburg, 35032, Germany

E-mail: jonas.koenig@physik.uni-marburg.de

S.1 Methods

S.1.1 Wannier equation

To obtain exciton energies and wavefunctions, we solve the Wannier equation¹

$$\sum_{\mathbf{k}'} \left(\frac{\hbar^2 k'^2}{2m_r} \delta_{\mathbf{k}\mathbf{k}'} + V_{|\mathbf{k}-\mathbf{k}'|} \right) \Psi_n(\mathbf{k}') = E_b^n(\mathbf{k}) \Psi_n(\mathbf{k}), \quad (\text{S.1})$$

where $m_r = 0.108m_e$ is the reduced mass of the electron and hole², V_q is the screened Coulomb potential, E_n are the exciton binding energies, and the corresponding wavefunctions are denoted by Ψ_n . The electron and hole masses are taken from Ref. 2 and the Keldysh approximation is used for the screened Coulomb potential³. The high-frequency dielectric constants of the organic spacer layer and the inorganic perovskite layer are set to⁴ 3.3 and 6.1, respectively. The thickness of the perovskite slab is set to⁴ 0.636 nm.

S.1.2 Exchange interaction and optical selection rules

Considering only the 1s exciton, the spin combination of the constituent electron and hole leads to four degenerate states. These states interact with each other through the exchange interaction, as well as with an applied magnetic field via the Zeeman effect, leading to the following eigenvalue problem in the exciton basis⁵

$$\begin{pmatrix} I_Z & -g_v(B) & g_c(B) & -I_Z \\ -g_v(B) & I_r & 0 & g_c(B) \\ g_c(B) & 0 & I_r & -g_v(B) \\ -I_Z & g_c(B) & -g_v(B) & I_Z \end{pmatrix} \begin{pmatrix} D_{\mu,\mathbf{q}}^{\uparrow\uparrow} \\ D_{\mu,\mathbf{q}}^{\uparrow\downarrow} \\ D_{\mu,\mathbf{q}}^{\downarrow\uparrow} \\ D_{\mu,\mathbf{q}}^{\downarrow\downarrow} \end{pmatrix} = E_{\mu,\mathbf{q}}^{(X)}(B) \begin{pmatrix} D_{\mu,\mathbf{q}}^{\uparrow\uparrow} \\ D_{\mu,\mathbf{q}}^{\uparrow\downarrow} \\ D_{\mu,\mathbf{q}}^{\downarrow\uparrow} \\ D_{\mu,\mathbf{q}}^{\downarrow\downarrow} \end{pmatrix}, \quad (\text{S.2})$$

where $I_{r(Z)}$ quantify both the short- and long-range exchange interaction strength in the in-plane (out-of-plane) direction of the perovskite. Furthermore, $g_{c/v}(B) = g_{c/v} \frac{\mu_B B}{2}$, and $g_c = 2.9$ and $g_v = -1.1$ denote the g-factors in the excitonic basis⁶. At zero magnetic field, the resulting excitonic fine structure states at $|\mathbf{q}| = 0$ are given by

$$E_D^{(X)} = \Delta + E_b^{1s}, \quad E_T^{(X)} = \Delta + E_b^{1s} + I_r, \quad E_L^{(X)} = \Delta + E_b^{1s} + I_r, \quad E_Z^{(X)} = \Delta + E_b^{1s} + 2I_Z,$$

where Δ is the bandgap energy. The respective eigenvectors are given by

$$D_D = \frac{1}{\sqrt{2}}(1, 0, 0, 1), \quad D_T = (0, 1, 0, 0), \quad D_L = (0, 0, 1, 0), \quad D_Z = \frac{1}{\sqrt{2}}(1, 0, 0, -1).$$

Here, we fit I_r and I_Z to the experimentally obtained values for the splitting between the dark (X_D) and bright states ($X_{T/L}$), as well as between the dark and gray state (X_Z)⁶.

The oscillator strength $|M_\sigma^\mu(\mathbf{B})|^2$ of each state is a linear combination of the dipole moments of each exciton, $\mathbf{d}_{ss'}^{cv}$, weighted by the respective eigenvector, and then projected

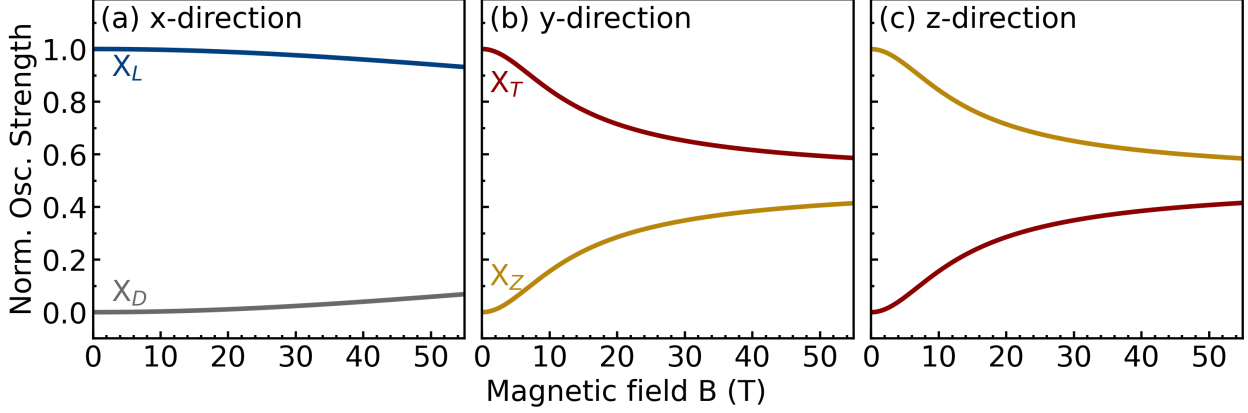


Figure S.1: (a) Oscillator strength in the x-direction of the excitonic fine structure states, X_D and X_L , polarized in the x-direction (longitudinal to the magnetic field). (b)-(c) Oscillator strength in the y-direction (transversal and in-plane) and the z-direction (transversal and out-of-plane) of the corresponding states, X_T and X_Z , respectively.

onto the polarization of the light⁵ \mathbf{e}_σ

$$|M_\sigma^\mu|^2(\mathbf{B}) \propto |\Psi_{1s}(\mathbf{r} = 0)|^2 |\mathbf{e}_\sigma \cdot \sum_{ss'} \mathbf{d}_{ss'}^{cv} D_\mu^{ss'}(\mathbf{B})|,$$

where $\Psi_{1s}(\mathbf{r})$ is the wavefunction in real space, and s (s') denotes the electron (hole) spin for the respective exciton. Without a magnetic field, the dark exciton state has a zero transition dipole moment, the two degenerate bright states are circularly polarized in the xy -plane, and the gray state is polarized along the out-of-plane z direction. The magnetic field mixes these states, leading to the modified selection rules, cf. Fig. 1 of the main text. The magnetic field dependence of the oscillator strength for different polarization orientations is shown in Fig S.1. In particular, Fig. S.1(a) illustrates the transfer of oscillator strength from the bright state X_L to the dark exciton X_D with increasing magnetic field. Figures S.1(b) and (c) show the mixing of the oscillator strength for the transverse state X_T and the out-of-plane gray exciton X_Z , due to the rotation of the respective transition dipole moments around the magnetic field axis (Fig. 1 in the main text). Note that for all magnetic fields, the total oscillator strength in each polarization direction is equal to unity.

S.1.3 Scattering matrix method

The scattering matrix (S-matrix) method is a numerical algorithm used to exactly solve Maxwell’s equations for stacks of dielectric slabs with in-plane translational invariance or periodicity⁷. It provides access to the optical response of the system for any incident light angle. However, it is difficult to disentangle photonic and material contributions of a mixed light-matter state, as described by Hopfield coefficients. In particular, this is necessary to obtain access to the different decay channels associated with the constituent excitons and cavity modes. To this end, we use a Hopfield model (see Eq. 3 in the main text) using parameters extracted from S-matrix simulations.

In this work, we consider a microcavity consisting of two $\lambda/4$ -DBR mirrors, each consisting of eight stacks of alternating SiO_2 and TaO_2 ($n_{\text{SiO}_2} = 1.46$ and $n_{\text{Ta}_2\text{O}_5} = 2.0770$ ⁸) dielectric slabs, for a total number of 16 layers per DBR. A sketch of the simulated cavity can

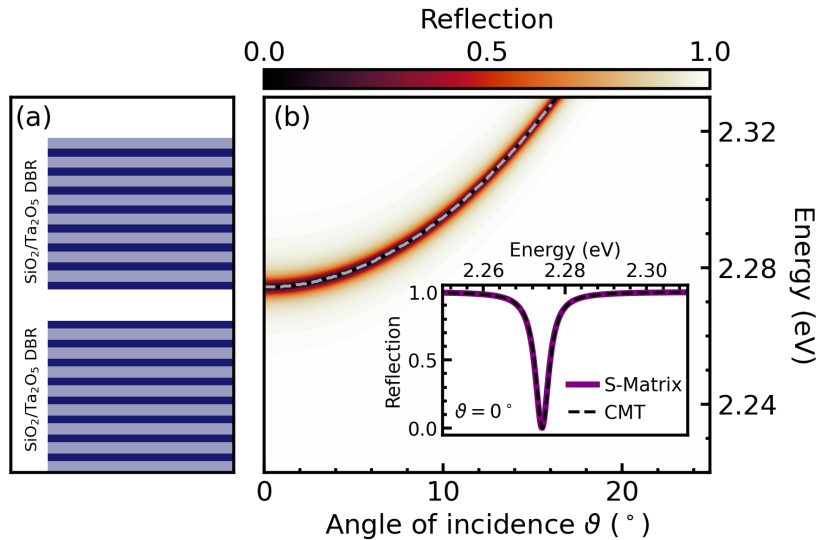


Figure S.2: (a) Schematic of the cavity used for the S-matrix simulations, constructed from two $\lambda/4$ -DBR mirrors, each consisting of alternating stacked SiO_2 (light blue) and TaO_2 (dark blue) layers. (b) S-matrix simulation of the reflection of the bare Fabry-Perot microcavity as a function of the photon energy and angle of incidence ϑ . The gray dashed line illustrates the extracted cavity photon mode energy, perfectly following the peak reflection. The inset shows a line cut at $\vartheta = 0^\circ$ (purple solid line) and the fit using coupled mode theory (black dashed line) with the extracted photon linewidth $\hbar\kappa$.

be seen in Fig. S.2(a). The thickness of the layers was chosen such that the center frequency of the DBR aligns with the energy of the dark state. To simulate and extract the cavity mode as a function of angle of incidence, we also have to include the dielectric background of the perovskite layer in the center of the cavity, i.e., without any excitonic effects. This is because a thin dielectric slab will affect the resonance condition of the microcavity. Using a dielectric background for the perovskite layer of 1.81⁹, we obtain the reflection of the cavity, as shown in Fig. S.2(b). By fitting a Lorentzian function to the reflection (Eq. S.5a in the limit of a bare cavity), we are able to obtain the cavity linewidth $\hbar\kappa$, see the inset of Fig. S.2(b). Including the dielectric tensor given in Eqs. (1) and (2) of the main text, we can calculate the optical response of the (PEA)₂PbI₄ perovskite layer integrated into the microcavity, and then extract the polariton energies from the dips in reflection. These energies are then fit to the Hopfield model in Eq. (3) of the main text to obtain access to the cavity photon-exciton coupling strengths and Hopfield coefficients.

S.1.4 Coupled mode theory

Assuming high Q-factor cavity modes and small material-based losses, coupled mode theory (CMT) provides an intuitive and simple description of the coupling between different modes of the system (excitons, cavity photons) and their coupling to external ports¹⁰. In particular, it provides insight into calculated absorption spectra via the critical coupling condition^{11–13}. Here, we detail the derivation of the polaritonic Elliott formula using classical two-port, two-resonator CMT equations. Starting from the Hamiltonian in Eq. (3) of the main text, we add an imaginary part to the exciton and cavity-photon energies on the diagonal to describe the respective loss parameters. We then obtain the following coupled dynamics of excitons

and cavity photons:

$$\partial_t \begin{pmatrix} C(t) \\ X_1(t) \\ X_2(t) \end{pmatrix} = -\frac{i}{\hbar} H \cdot \begin{pmatrix} C(t) \\ X_1(t) \\ X_2(t) \end{pmatrix} = \begin{pmatrix} -i\omega^{(C)} + \kappa & -i\frac{g_1}{\hbar} & -i\frac{g_2}{\hbar} \\ -i\frac{g_1}{\hbar} & -i\omega_1^{(X)} + \Gamma & 0 \\ -i\frac{g_2}{\hbar} & 0 & -i\omega_2^{(X)} + \Gamma \end{pmatrix} \cdot \begin{pmatrix} C(t) \\ X_1(t) \\ X_2(t) \end{pmatrix}$$

Here, $X_\mu(t)$ is the mode amplitude of the μ th exciton oscillating in time with the frequency $\omega_\mu^{(X)}$ and decay rate Γ . Furthermore, $C(t)$ is the amplitude of the cavity photon at the frequency $\omega^{(C)}$ with the decay rate κ . Using the Hopfield transformation^{14,15} $C(t) = \sum_n P_n(t)U_0^n$ and $X_\mu(t) = \sum_n P_n(t)U_\mu^n$, we can decouple the dynamics into a set of independent differential equations. Here, $P_n(t)$ is the polariton mode amplitude of the n th branch with U_0^n and U_μ^n as the respective photonic and excitonic Hopfield coefficients.

Next, we add the coupling to external photons, i.e., the two ports corresponding to the continuum of photon states in the half-space either side of the cavity^{10,15}. In a Fabry-Perot microcavity, only the photonic component of each polariton branch can couple to the ports, i.e., excitons are not directly excited by external photons. The incoming and outgoing waves are given by

$$(b^+)^T(t) = (b_1^+(t), b_2^+(t)), \quad (b^-)^T(t) = (b_1^-(t), b_2^-(t)), \quad (\text{S.3})$$

where $b_i^{-(+)}$ is the incoming (outgoing) wave at the i th port, as shown in Fig. S.3. The

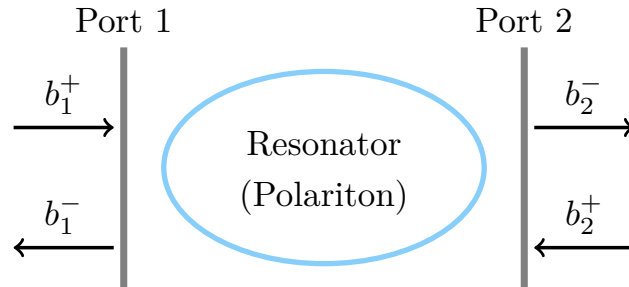


Figure S.3: Schematic of the ports 1 and 2 coupling the respective incoming waves (b_1^+ , b_2^+) and outgoing waves (b_1^- , b_2^-) to the resonator, i.e., the polariton.

incoming waves couple to the photonic part of the polaritons through $\xi_n^T = (\xi_{n,1}, \xi_{n,2})$ for each port respectively, while the outgoing waves couple via $d_n^T = (d_{n,1}, d_{n,2})$. The direct process of the incoming waves coupling to the outgoing waves is described by a 2×2 matrix \mathcal{C} . As direct transmission is not possible in an idealized Fabry-Perot cavity, we can only couple b_i^+ to b_i^- of the same port via reflection. Therefore, the matrix \mathcal{C} is the negative of the identity matrix. Note that one can also add the coupling to the ports before performing the Hopfield transformation and obtain the same equations.

Exploiting time-reversal symmetry^{10,16}, which is valid for low absorptive losses, we obtain

$$\xi_n = d_n = \begin{pmatrix} \sqrt{2\gamma_{n,1}^{(P)}} \\ \sqrt{2\gamma_{n,2}^{(P)}} \end{pmatrix},$$

where $\gamma_{n,i}^{(P)}$ is the photonic decay rate of the n th polariton branch into the i th port. The sum of the polaritonic radiative decay rate into each port is equal to the total photonic-based polariton decay rate from the main text, i.e., $\gamma_{n,1}^{(P)} + \gamma_{n,2}^{(P)} = \gamma_n^{(P)}$. This results in the polariton dynamics

$$\partial_t P_n(t) = (-i\omega_n - \gamma_n^{(P)} - \Gamma_n^{(P)}) P_n(t) + \sqrt{2\gamma_{n,1}^{(P)}} b_1^+(t) + \sqrt{2\gamma_{n,2}^{(P)}} b_2^+(t), \quad (\text{S.4a})$$

$$\begin{pmatrix} b_1^-(t) \\ b_2^-(t) \end{pmatrix} = \begin{pmatrix} -b_1^+(t) \\ -b_2^+(t) \end{pmatrix} + \sum_n \begin{pmatrix} \sqrt{2\gamma_{n,1}^{(P)}} \\ \sqrt{2\gamma_{n,1}^{(P)}} \end{pmatrix} P_n(t), \quad (\text{S.4b})$$

where ω_n and $\Gamma_n^{(P)}$ are the frequency and material-based decay rates of the n th polariton branch, and $b_i^{+(-)}$ are the incoming (outgoing) fields of the i th port. The first equation describes how polaritons are excited by the incoming waves, while the second equation expresses the emission of the outgoing waves.

As we consider only excitations from one port, we set $b_2^+(t) = 0$. For well-spaced polaritons, we can ignore any overlap and therefore solve the equations independently for one

polariton branch, and then simply add the final contributions together to obtain the total linear optical spectra. The Fourier transformation of Eqs. S.4a and S.4b gives the reflection and transmission coefficients for each polariton branch:

$$r_n(\omega) = \frac{b_1^-(\omega)}{b_1^+(\omega)} = \frac{-i(\omega - \omega_n) + \left(\gamma_{n,1}^{(P)} - \gamma_{n,2}^{(P)} - \Gamma_n^{(P)}\right)}{i(\omega_n - \omega) + \gamma_n^{(P)} + \Gamma_n^{(P)}} ,$$

$$it_n(\omega) = \frac{b_2^-(\omega)}{b_1^+(\omega)} = \frac{2\sqrt{\gamma_{n,1}^{(P)}\gamma_{n,2}^{(P)}}}{i(\omega_n - \omega) + \gamma_n^{(P)} + \Gamma_n^{(P)}} ,$$

In the limit of a symmetric cavity, the reflection, transmission, and absorption for each polariton branch are then given by

$$R_n(\omega) = \frac{(\omega_n - \omega)^2 + \left(\Gamma_n^{(P)}\right)^2}{(\omega_n - \omega)^2 + \left(\gamma_n^{(P)} + \Gamma_n^{(P)}\right)^2} , \quad (\text{S.5a})$$

$$T_n(\omega) = |it(\omega)|^2 = \frac{\left(\gamma_n^{(P)}\right)^2}{(\omega_n - \omega)^2 + \left(\gamma_n^{(P)} + \Gamma_n^{(P)}\right)^2} , \quad (\text{S.5b})$$

$$A_n(\omega) = 1 - R(\omega) - T(\omega) = \frac{2\gamma_n^{(P)}\Gamma_n^{(P)}}{(\omega_n - \omega)^2 + \left(\gamma_n^{(P)} + \Gamma_n^{(P)}\right)^2} , \quad (\text{S.5c})$$

resulting in the polaritonic Elliott formula (Eq. 4 of the main text). These equations also apply to the case of a bare Fabry-Perot cavity by setting $\Gamma_n^{(P)} = 0$ and replacing $\gamma_n^{(P)}$ with the bare cavity decay rate κ . This allows us to fit and extract the cavity photon linewidth from the S-matrix simulation, as shown by the black dashed curve in the inset of Fig.S.2. Furthermore, in the excitonic limit, $\Gamma^{(P)} = \Gamma$ and $\gamma^{(P)} = \gamma$, with γ being the radiative decay rate of the exciton, equation S.5c gives the well-known excitonic Elliott formula¹⁷. In this case, excitons can couple directly to the ports, rather than indirectly via cavity photons. The Elliott formula reveals that the maximum absorption of 0.5 at resonance is reached when the critical coupling condition $\Gamma_n^{(P)} = \gamma_n^{(P)}$ is met^{11-13,15}.

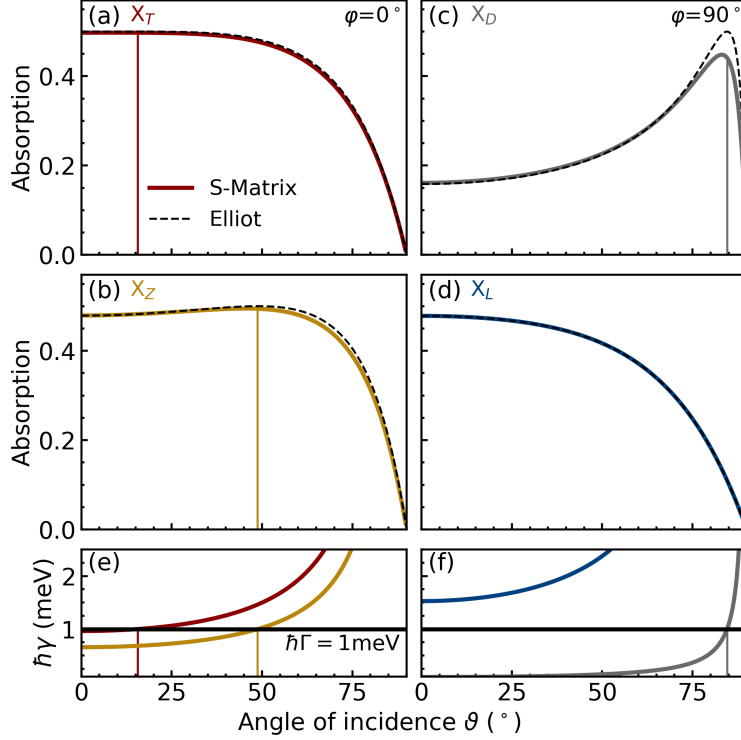


Figure S.4: (a)-(d) Absorption of a $(\text{PEA})_2\text{PbI}_4$ perovskite layer as a function of the angle of incidence, ϑ , resonant with the four exciton fine structure states X_T , X_Z , X_D and X_L calculated using the S-matrix method (colored solid lines) and the Elliott formula (black dashed lines). (e)-(f) Radiative decay of the respective states (colored lines) and material-based loss (black horizontal line) as a function of ϑ for the states shown in (a)-(d), respectively. The colored vertical lines illustrate, where the excitonic decay rate equals the respective photonic decay, i.e., where the critical coupling condition is met resulting in a maximum absorption.

Comparing the absorption of the single perovskite layer between the S-matrix method and the Elliott formula in Fig. S.4, we find excellent agreement for all states. The minor deviation reflects a small spectral overlap between the X_T and X_Z excitons, which is not taken into account in the Elliott formula. Additionally, we find that the critical coupling condition fully describes the absorption behavior, as illustrated by the vertical colored lines in Fig. S.4.

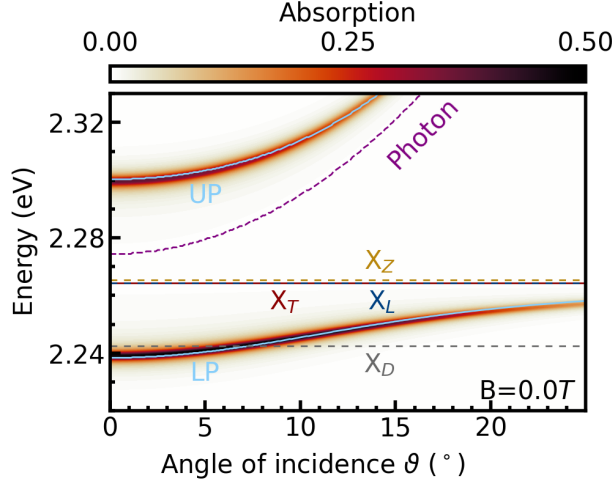


Figure S.5: Absorption of a 2D $(\text{PEA})_2\text{PbI}_4$ perovskite layer integrated within a Fabry-Perot microcavity as a function of the photon energy and angle of incidence at $B = 0$ T. The dashed horizontal lines denote the energy of the different excitonic states. As only the degenerate bright states X_T and X_L can couple to the light (due to the selection rules shown in Fig. S.1), only two polariton branches, LP and UP, are visible with a fully dark middle polariton branch lying on top of the two degenerate states. As there is no breaking of in-plane symmetry, the absorption spectrum is independent of the azimuth angle.

S.2 Polariton landscape

Without a magnetic field, only the two circularly polarized bright states X_T and X_L can couple to the TE-polarized light, as shown in Figs. S.1(a)-(b). Therefore, only two azimuth-angle-independent polariton branches are visible in absorption, cf. Fig. S.5. In other words, the polariton dispersion is isotropic in the absence of a magnetic field. These two branches are equivalent to the polaritons visible in Fig. 3(a) of the main text, showing a single large Rabi splitting centered on X_T . This is because even at $B = 50$ T, the two transversally polarized states X_T and X_Z are still almost degenerate in energy and have together the same in-plane oscillator strength as X_T at $B = 0$ T due to the conservation of oscillator strength, cf. Fig. S.1(b).

The dependence of the polariton landscape on the magnetic field strength is shown in Fig. S.6. Similar to Fig. 3 in the main text, it reveals a single branch (LP) around the energy of the dark state at $\varphi = 0^\circ$, two at $\varphi = 90^\circ$ (LP' and MP') and a superposition of the two

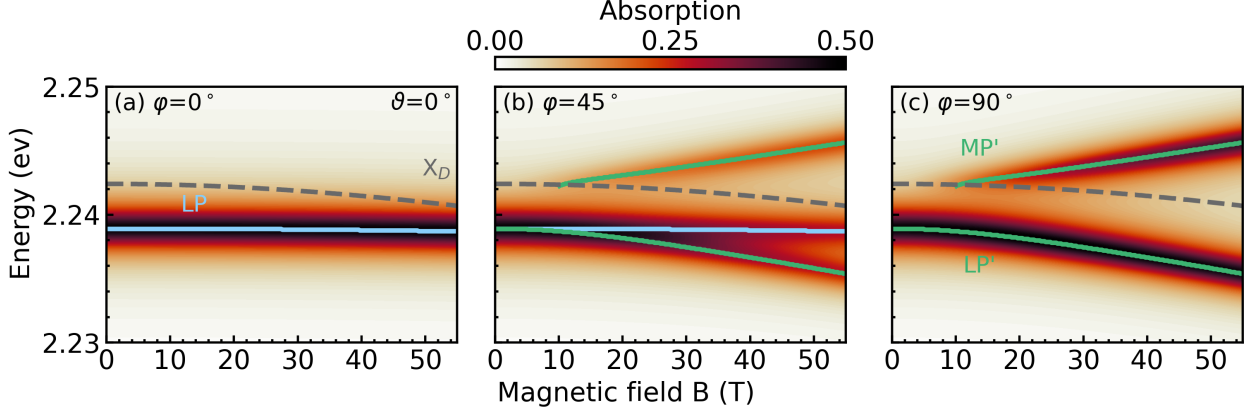


Figure S.6: (a)-(c) Absorption of a 2D $(\text{PEA})_2\text{PbI}_4$ perovskite layer integrated within a Fabry-Perot microcavity as a function of the photon energy and magnetic field strength B , for $\vartheta = 0^\circ$, and for three different azimuth angles $\varphi = 0^\circ$, 45° , and 90° . The dashed line denotes the energy of the dark state X_D . As the latter can not couple to light at $\varphi = 0^\circ$, according to the selection rules, only a single polariton branch (LP) stemming from the energetically higher bright states can be observed in this energy range. In contrast, for $\varphi = 90^\circ$, the dark state can couple to the cavity mode, and therefore two branches appear (LP' and MP').

edge cases at $\varphi = 45^\circ$ with approximately halved absorption. The MP' branch can only be resolved starting at about 10 T because, below this field strength, the dark state lacks sufficient oscillator strength to enter the strong coupling regime, i.e., $g < (\hbar\gamma + \hbar\Gamma)/2$. The energies of LP' and MP' polaritons are used to calculate the Rabi splitting around the dark state as a function of B , shown in Fig. 4(a) of the main text.

S.3 Hopfield coefficients

The Hopfield coefficients for the polariton branches shown in Fig. S.7 of the main text are obtained by fitting the Hopfield/CMT model to the reflection spectrum. Both lower branches, LP and LP', have the highest contribution from their respective excitons in the small-incident-angle limit, while in the high-angle limit, they become almost fully photonic. The two upper branches, UP and UP' show the opposite behavior: they possess the highest photonic contribution at small angles and are almost fully excitonic at high angles¹⁵. For $\varphi = 0^\circ$, the middle polariton branch, MP, has a negligible photonic component and therefore

appears flat and almost dark, cf. Fig. 3(a) of the main text. In contrast, the MP' branch for $\varphi = 90^\circ$ exhibits a photonic component and thus has a sizable absorption (Fig. 3(c) of the main text). These Hopfield coefficients at normal incidence, $\vartheta = 0^\circ$, are used to obtain the excitonic and radiative linewidths $\hbar\Gamma_n^{(P)}$ and $\hbar\gamma^{(P)}$, which help further understand the absorption shown in Fig. 4 of the main text.

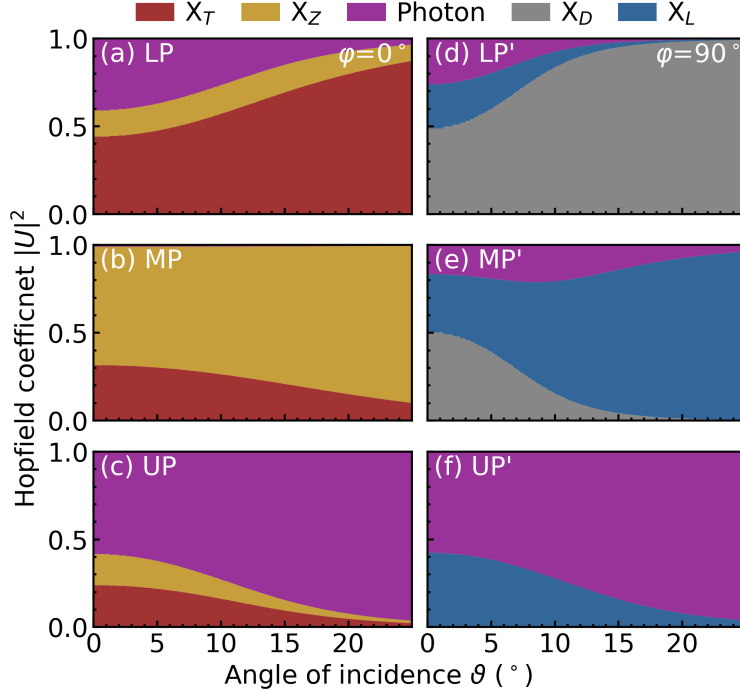


Figure S.7: Hopfield coefficients as a function of angle of incidence, ϑ , for the polariton branches shown in Figs. 3(a) and (c) of the main text. They describe the excitonic and photonic composition of these branches.

References

- (1) Brem, S.; Selig, M.; Berghaeuser, G.; Malic, E. Exciton relaxation cascade in two-dimensional transition metal dichalcogenides. *Scientific reports* **2018**, *8*, 1–8.
- (2) Ziegler, J. D.; Zipfel, J.; Meisinger, B.; Menahem, M.; Zhu, X.; Taniguchi, T.; Watanabe, K.; Yaffe, O.; Egger, D. A.; Chernikov, A. Fast and anomalous exciton diffusion in two-dimensional hybrid perovskites. *Nano Letters* **2020**, *20*, 6674–6681.

- (3) Feldstein, D.; Perea-Causin, R.; Wang, S.; Dyksik, M.; Watanabe, K.; Taniguchi, T.; Plochocka, P.; Malic, E. Microscopic picture of electron–phonon interaction in two-dimensional halide perovskites. *The Journal of Physical Chemistry Letters* **2020**, *11*, 9975–9982.
- (4) Hong, X.; Ishihara, T.; Nurmikko, A. Dielectric confinement effect on excitons in PbI₄-based layered semiconductors. *Physical Review B* **1992**, *45*, 6961.
- (5) Thompson, J. J.; Dyksik, M.; Peksa, P.; Posmyk, K.; Joki, A.; Perea-Causin, R.; Erhart, P.; Baranowski, M.; Loi, M. A.; Plochocka, P.; others Phonon-Bottleneck Enhanced Exciton Emission in 2D Perovskites. *Advanced Energy Materials* **2024**, *14*, 2304343.
- (6) Dyksik, M.; Duim, H.; Maude, D. K.; Baranowski, M.; Loi, M. A.; Plochocka, P. Brightening of dark excitons in 2D perovskites. *Science advances* **2021**, *7*, eabk0904.
- (7) Rumpf, R. C. Improved formulation of scattering matrices for semi-analytical methods that is consistent with convention. *Progress In Electromagnetics Research B* **2011**, *35*, 241–261.
- (8) Rodríguez-de Marcos, L. V.; Larruquert, J. I.; Méndez, J. A.; Aznárez, J. A. Self-consistent optical constants of SiO₂ and Ta₂O₅ films. *Optical Materials Express* **2016**, *6*, 3622–3637.
- (9) Fieramosca, A.; De Marco, L.; Passoni, M.; Polimeno, L.; Rizzo, A.; Rosa, B. L.; Cruciani, G.; Dominici, L.; De Giorgi, M.; Gigli, G.; others Tunable out-of-plane excitons in 2D single-crystal perovskites. *Acs Photonics* **2018**, *5*, 4179–4185.
- (10) Fan, S.; Suh, W.; Joannopoulos, J. D. Temporal coupled-mode theory for the Fano resonance in optical resonators. *JOSA A* **2003**, *20*, 569–572.

- (11) Ferreira, B.; Rosati, R.; Fitzgerald, J. M.; Malic, E. Signatures of dark excitons in exciton–polariton optics of transition metal dichalcogenides. *2D Materials* **2022**, *10*, 015012.
- (12) König, J. K.; Fitzgerald, J. M.; Hagel, J.; Erkensten, D.; Malic, E. Interlayer exciton polaritons in homobilayers of transition metal dichalcogenides. *2D Materials* **2023**, *10*, 025019.
- (13) Ferreira, B.; Shan, H.; Rosati, R.; Fitzgerald, J. M.; Lackner, L.; Han, B.; Esmann, M.; Hays, P.; Leibelng, G.; Watanabe, K.; Taniguchi, T.; Eilenberger, F.; Tongay, S.; Schneider, C.; Malic, E. Revealing Dark Exciton Signatures in Polariton Spectra of 2D Materials. *ACS Photonics* **2024**, *11*, 2215–2220.
- (14) Hopfield, J. Theory of the contribution of excitons to the complex dielectric constant of crystals. *Physical Review* **1958**, *112*, 1555.
- (15) Fitzgerald, J. M.; Thompson, J. J.; Malic, E. Twist angle tuning of moiré exciton polaritons in van der Waals heterostructures. *Nano Letters* **2022**, *22*, 4468–4474.
- (16) Zhao, Z.; Guo, C.; Fan, S. Connection of temporal coupled-mode-theory formalisms for a resonant optical system and its time-reversal conjugate. *Physical Review A* **2019**, *99*, 033839.
- (17) Kira, M.; Koch, S. W. Many-body correlations and excitonic effects in semiconductor spectroscopy. *Progress in quantum electronics* **2006**, *30*, 155–296.